Journal of Colloid and Interface Science 660 (2024) 401–411

Contents lists available at ScienceDirect

Journal of Colloid And Interface Science

journal homepage: www.elsevier.com/locate/jcis

Regular Article

Exploring the synergistic effect of palladium nanoparticles and highly dispersed transition metals on carbon nitride/super-activated carbon composites for boosting electrocatalytic activity

G. Alemany-Molina [a], M. Navlani-García [a], J. Juan-Juan [b], E. Morallón [c], D. Cazorla-Amorós [a,*]

[a] Department of Inorganic Chemistry and Materials Institute, University of Alicante, Ap. 99, Alicante E-03080, Spain
[b] Research Support Services, University of Alicante, Ap. 99, Alicante E-03080, Spain
[c] Department of Physical Chemistry and Materials Institute, University of Alicante, Ap. 99, Alicante E-03080, Spain

GRAPHICAL ABSTRACT

Outstanding performance of multifunctional electrocatalysts based on Pd nanoparticles and highly dispersed transition metals on C3N4/super-activated carbon composites towards the OER, HER and ORR explored by experimental and DFT calculations.

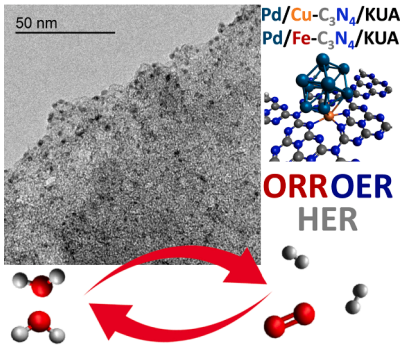

ARTICLE INFO

Keywords:
Carbon nitride
Copper
Iron
Palladium
HER
ORR
OER

ABSTRACT

In the present work, multifunctional electrocatalysts formed by palladium nanoparticles (Pd NPs) loaded on Fe or Cu-containing composite supports, based on carbon nitride (C_3N_4) and super-activated carbon with a high porosity development (S_{BET} 3180 m^2/g, V_{DR} 1.57 cm^3/g, and V_T 1.65 cm^3/g), were synthesised. The presence of Fe or Cu sites favoured the formation of Pd NPs with small average particle size and a very narrow size distribution, which agreed with Density Functional Theory (DFT) calculations showing that the interaction of Pd clusters with C_3N_4 flakes is weaker than with Cu- or Fe-C_3N_4 sites. The electroactivity was also dependent on the composition and, as suggested by preliminary DFT calculations, the Pd-Cu catalyst showed lower overpotential for hydrogen evolution reaction (HER) while bifunctional oxygen reduction reaction/ oxygen evolution reaction (ORR/OER) behaviour was superior in Pd-Fe sample. The Pd-Fe electrocatalyst was studied in a zinc-air battery (ZAB) for 10 h, showing a performance similar to a commercial Pt/C + RuO_2 catalyst with a high content of precious metal. This study demonstrates the synergistic effect between Pd species and transition metals and

* Corresponding author.
E-mail address: cazorla@ua.es (D. Cazorla-Amorós).

https://doi.org/10.1016/j.jcis.2024.01.057
Received 1 November 2023; Received in revised form 13 December 2023; Accepted 8 January 2024
Available online 11 January 2024

shows that transition metals anchored on C_3N_4-based composite materials promote the electroactivity of Pd NPs in HER, ORR and OER due to the interaction between both species.

1. Introduction

The development of new cost-effective materials for electrocatalytic applications remains an important bottleneck to achieving a carbon-emission-free and sustainable energy model. Fuel cells (FC) and electrolysers (EC) are emerging as potential devices to produce and consume green hydrogen on a large scale [1]. However, the dependence of renewable energies on discontinuous sources (solar, wind, hydropower, etc.) demands more flexible systems able to couple conversion and storage of energy. Due to the limitations of Li-ion batteries in terms of storage timescale and amount of power stored [2], hydrogen ion batteries (regenerative fuel cells (RFC)) and metal-air flow batteries, especially zinc-air (ZABs) in basic medium, have emerged as the most promising alternatives [3–5].

Oxygen reduction reaction (ORR) occurs at the cathode of FC or RFC in fuel cell mode and during the discharge process of metal-air batteries. To obtain high activities, catalysts based on elevated contents of Pt supported on carbon materials are required to overcome the sluggish kinetics of ORR, while much lower contents of Pt (0.05 mg Pt cm^{-2}) are required for hydrogen oxidation reaction (HOR) occurring in the anode [6–8]. When the RFC device works in the electrolysis mode, hydrogen evolution reaction (HER) takes place in the cathode and oxygen evolution reaction (OER) in the anode, which also occurs in the charging process of metal-air batteries. Catalysts based on Pt and metals of the Pt-group (Ru, Rh, Ir and Pd) are considered as the materials with lower overpotential for HER, but the high prices and the scarcity of these metals limit accomplishing a large-scale application [9,10]. On the other hand, OER is limited by the oxidation of carbon supports and the deactivation of the catalysts after some cycles due to metal leaching [11]. Furthermore, bifunctional catalysts required in RFC and metal-air batteries also need active metal phases towards the ORR [4,5].

The scarcity and high cost of Pt motivate the search for alternative catalysts such as metal-free and non-noble metal-based catalysts [12,13]. Even though great achievements have been reported with these alternative electrocatalysts, they do not meet the requirements in terms of activity and stability. Against this background, Pd, which has similar properties to Pt, and a historically lower cost than Pt, is a very promising alternative active phase for electrocatalysis. However, the increasing cost of Pd in the last years has boosted the research community to focus on achieving maximum atomic efficiency by designing advanced electrocatalysts with tailored properties and active phase engineering [14–18].

Materials based on Pd NPs have shown great performance for the reactions mentioned above in an alkaline medium [19–23]. However, the Department of Energy (DOE) of the U.S. states that electrodes for FCs should not exceed the 0.125 mg cm^{-2} loading of Pt group metals (PGM) [24]. To minimise the amount of noble metal used and promote catalytic performance, strategies such as alloying with other metals or reducing the active phase size have been widely used in the last years in heterogeneous catalysis [25–28]. Following these strategies, it has been recently reported that Fe—N—C sites can act as nucleation and growth centres for Pd NPs [29]. The reduction of the size of the NPs can originate higher activities or even different selectivity [30–32]. Also, alloying noble metals with transition metals alters the electronic properties due to the modification of the chemical environment [29].

As for the support, carbon nitride (C_3N_4) has recently received great attention for many catalytic/electrocatalytic processes [33]. It is well-known that C_3N_4 itself is not electrocatalytically active [34], but suitable engineering of metal-C_3N_4 sites has resulted in materials with excellent performance in electrocatalytic processes. In this sense, C_3N_4 contains multiple N sites, which serve as strong metal anchoring sites, which is particularly important in attaining highly dispersed metal species [33,35–37].

However, the low surface of C_3N_4, together with its layered stacked structure, limits somehow the potential anchoring effect. That can be circumvented by combining C_3N_4 with carbon materials forming hybrids or composite materials to enhance textural properties [13,38–40]. The materials developed in this study are formed by domains of amorphous C_3N_4 which are loaded on the activated carbon with well-developed porosity. Such activated carbon serves as a platform for the efficient formation of C_3N_4 domains so that maximum availability of the *N*-anchoring sites is achieved.

The highly dispersed metal sites afford high atomic efficiency, and they normally possess superior catalytic performance due to their minimal size. In the present study, C_3N_4 did not only serve to achieve highly dispersed transition metals (M−C_3N_4), but M−C_3N_4 sites also favoured the formation of small and well-dispersed Pd NPs. However, the benefits of C_3N_4 are not limited to such strong metal-support interaction, but also to the good electron donation and acceptance ability of the pyridinic nitrogen present in the C_3N_4 structure, which is also a key aspect in catalytic/electrocatalytic processes [41].

Motivated by the interesting results achieved in our previous studies [13,42], in this work, we designed multifunctional electrocatalysts based on a very low content of noble metals by exploring the synergistic effect between highly dispersed Fe or Cu species, anchored on composite materials based on C_3N_4 and an activated carbon with high porosity development (BET surface area > 3000 m^2 g^{-1}), and Pd NPs. We also provide some additional fundamental insights about the synergy between Pd and a non-noble transition metal that modifies the catalytic activity. Furthermore, besides the important modifications of the catalytic activity, covering the highly dispersed Fe-N_x sites with Pd NPs is demonstrated to be a very interesting strategy to prevent Fe leaching and extend the durability of these electrocatalysts in ORR. The activated carbon allowed to maximise the availability of surface Lewis basic sites of C_3N_4, which ensures the presence of homogeneous and highly dispersed transition metal active sites. Then, Pd NPs were synthesised over the composite materials and the physicochemical properties and catalytic activity of the resulting electrocatalysts were studied. Furthermore, DFT calculations were applied to obtain some insights into the interaction and performance of the transition metal - Pd NP sites. It should be noted that, to the best of our knowledge, transition metals anchored on carbon-based materials have not been studied before to promote the electroactivity of Pd NPs in HER, ORR and OER.

2. Experimental

2.1. Materials

Information on the materials used in the synthesis is detailed in the supporting information.

2.2. M−C3N4/KUA And Pd/M−C3N4/KUA synthesis

The support (activated carbon denoted as KUA) was prepared by chemical activation of anthracite with KOH and following the procedure described elsewhere [43]. The experimental steps followed for the preparation of M−C3N4/KUA and Pd/M−C3N4/KUA are explained in the supporting information.

2.3. Physicochemical characterisation

The as-synthesised materials were characterised by means of several

physicochemical characterisation techniques. All the information as well as error estimates can be found in the supporting information.

2.4. Density functional theory (DFT) calculations

Density functional theory (DFT) simulations were carried out to support the observed experimental results. The details about DFT simulations are included in the supporting information.

2.5. Electrochemical characterisation

Electrochemical characterisation of the samples was performed by cyclic voltammetry in a three-electrode cell. The electrochemical behaviour of the developed electrocatalysts for the ORR, HER and OER was assessed. Zinc-air battery (ZAB) experiments were also performed, using the device shown in Figure S1. All the experimental details and error estimated are included in the supporting information.

3. Results and discussion

3.1. Characterisation of the samples

The nitrogen and metals (i.e., Pd, Fe, and Cu) content was obtained from EA and ICP, respectively (Table 1). Although C3N4/KUA and M−C3N4/KUA samples were prepared with the same amount of dicyandiamide, the final content of N in the composite material was higher for those M−C3N4/KUA samples than for the metal-free counterpart, which can be explained by the fact that the synthesis of C_3N_4 can be favoured in presence of transition metals [44]. The atomic N/M ratio derived from EA and ICP characterisation was 7.9 and 6.5 for Cu-C3N4/KUA and Fe-C3N4/KUA, respectively.

XRD patterns of the synthesised samples are included in Fig. 1a. The figure also includes the diffractogram of bare C_3N_4 for comparison purposes. C_3N_4 presented an intense peak centred at 27° due to the reflection from the plane (0 0 2) of graphitic carbon nitride (g-C_3N_4) and a small peak at 13° that corresponds to the (1 0 0) plane [38,45]. These contributions were not observed in the as-prepared samples, which means that no large sheets of C_3N_4 were obtained but amorphous C_3N_4-type nanodomains may have been formed inside the abundant porosity of the activated carbon. M−C3N4/KUA samples did not present diffraction peaks assignable to the metal species. The diffractogram of Cu-C3N4/KUA did not show peaks related to the presence of Cu species, which suggested that Cu-C3N4/KUA may not contain NPs larger than 2 nm, but smaller nanoparticles or single atoms, which was confirmed by TEM analysis (*vide infra*). For Fe-C3N4/KUA sample, a small peak at 36.0° may be related to Fe atoms forming some iron oxide nanoparticles [38,46,47]. Small peaks at 40.1°, 48.0° and 68.8° in Pd/C3N4/KUA sample can be associated with the (1 1 1), (2 0 0) and (2 2 0) reflections from Pd particles, respectively, indicating that Pd NPs were detected in that sample [48]. Interestingly, these small peaks were not observed in Pd/M−C3N4/KUA samples. The absence of those signals in Pd/M−C3N4/KUA samples confirmed that an important decrease of the Pd NPs size took place due to the presence of Fe or Cu, indicating that a better dispersion of Pd species was achieved when those transition metals were present in the materials (results confirmed by TEM, *vide infra*).

Table 1
Nitrogen content (%N (at.%) EA), metallic content (%M ICP (wt%)), and textural properties.

Catalyst	% N (at. %) EA	%M ICP (wt %)*	S_{BET} (m^2/g)	V_{DR} (cm^3/g)	V_T (cm^3/g)
KUA	–	–	3180	1.57	1.65
C3N4/KUA	1.6	–	3090	1.52	1.57
Cu-C3N4/KUA	2.3	1.5 / -	3000	1.49	1.54
Fe-C3N4/KUA	1.9	1.3 / -	3030	1.52	1.57
Pd/C3N4/KUA	1.7	- / 1.0	2830	1.21	1.46
Pd/Cu-C3N4/KUA	2.3	1.4 / 0.8	2830	1.21	1.43
Pd/Fe-C3N4/KUA	2.0	1.1 / 0.9	2870	1.25	1.51

* Fe or Cu / Pd.

The morphology of the developed samples was analysed by FESEM. As can be seen in Fig. 1b and Fig. S3, the samples correspond to low crystallinity activated carbon materials and no significant differences can be observed between KUA and the catalysts prepared. This fact can be related to the formation of small and well-distributed C_3N_4 domains.

TPR-H_2 experiments are presented in Fig. 1c. The results show interesting differences among the materials. Interestingly, the amount of H_2 consumed by the samples containing Pd is more than 10 times higher than the amount of Pd loaded in the materials (considering that it is as Pd^{2+}). This means that, after Pd reduction, the metal species are catalysing H_2 dissociation and further reaction with the carbon surface, as has been previously reported elsewhere [49]. While Pd/C3N4/KUA showed a broad hydrogen consumption peak due to the wide particle size distribution (*vide infra*), Pd/M−C3N4/KUA samples presented a more localised and narrow hydrogen consumption that proves the effective interaction between Pd and M−C_3N_4 species.

The results of nitrogen adsorption–desorption isotherms are included in Fig. 1d and Table 1 summarises the porous texture data of all the samples. The microporous character of the samples was observed since the adsorption isotherms are of Type I. The pristine activated carbon presents excellent textural properties with a S_{BET} over 3000 $m^2\ g^{-1}$. The presence of domains of C_3N_4 slightly decreases the surface area but the highly dispersed transition metals have an almost negligible effect in the apparent surface area. The incorporation of 1 wt% of Pd slightly decreased the S_{BET} and V_{DR}. Interestingly, the textural properties of Pd/C3N4/KUA and Pd/M−C3N4/KUA samples were very similar (Table 1), and the excellent textural properties of pristine KUA activated carbon were preserved due to the good dispersion of both C_3N_4 domains and Pd NPs.

N 1 s XPS spectra are shown in Fig. S4. Three contributions can be distinguished in the N 1 s XPS spectrum of bare C_3N_4. The first peak centred at 398.6 eV is related to the presence of sp^2 nitrogen atoms of the triazine and heptazine rings in the C_3N_4 structure. The peak located at ~ 399.8 eV is attributed to the nitrogen atoms that bond the heptazine units and terminal amine groups. The peak centred at 401.0 eV is assigned to quaternary or positively charged nitrogen atoms. Such contribution usually appears in N 1 s spectra because of the X-ray irradiation [45,50]. As can be seen in Fig. S4, M−C3N4/KUA and Pd/M−C3N4/KUA samples showed the same contributions as C_3N_4. Nevertheless, some differences were seen, especially for the peak centred at ~ 399.8 eV. The contribution of this peak to the spectra was slightly higher when metals are present. This is coherent with the presence of M−N bonds, which present a contribution at ~ 399.5 eV [51] that may be overlapping with the central peak.

Fig. 1e contains the XPS spectra of Fe, Cu, and Pd, registered for the different catalysts. Fe $2p_{3/2}$ spectra were deconvoluted with a multiplet of 4 peaks (according to Grosvenor et al. [52]) corresponding to Fe^{3+}, centred at 709.8, 710.7, 711.4, and 712.3 eV. Also, a satellite peak appears at 715 eV [52]. Neither Fe^{2+} (located at 709.6 eV and 53.7 eV for 2p and 3p regions, respectively) nor Fe^0 (located at 706.7 and 53.0 eV for 2p and 3p regions, respectively) were observed for Fe-C3N4/KUA and Pd/Fe-C3N4/KUA. That indicated that the iron species present in the catalysts have the same oxidation state as in the metal precursor used in the synthesis. That result is coherent with the Ellingham diagram of iron and considering the carbonisation temperature used in the presence of carbon [53]. Nevertheless, Cu-C3N4/KUA showed a considerable percentage of reduced copper. The Cu $2p_{3/2}$ spectra can be deconvoluted in two contributions [54–56]. The first peak corresponds to Cu^+ (or Cu^0) and the second contribution at 934.7 eV is associated with Cu^{2+}. Interestingly, when Pd NPs are loaded (Pd/Cu-C3N4/KUA sample), the

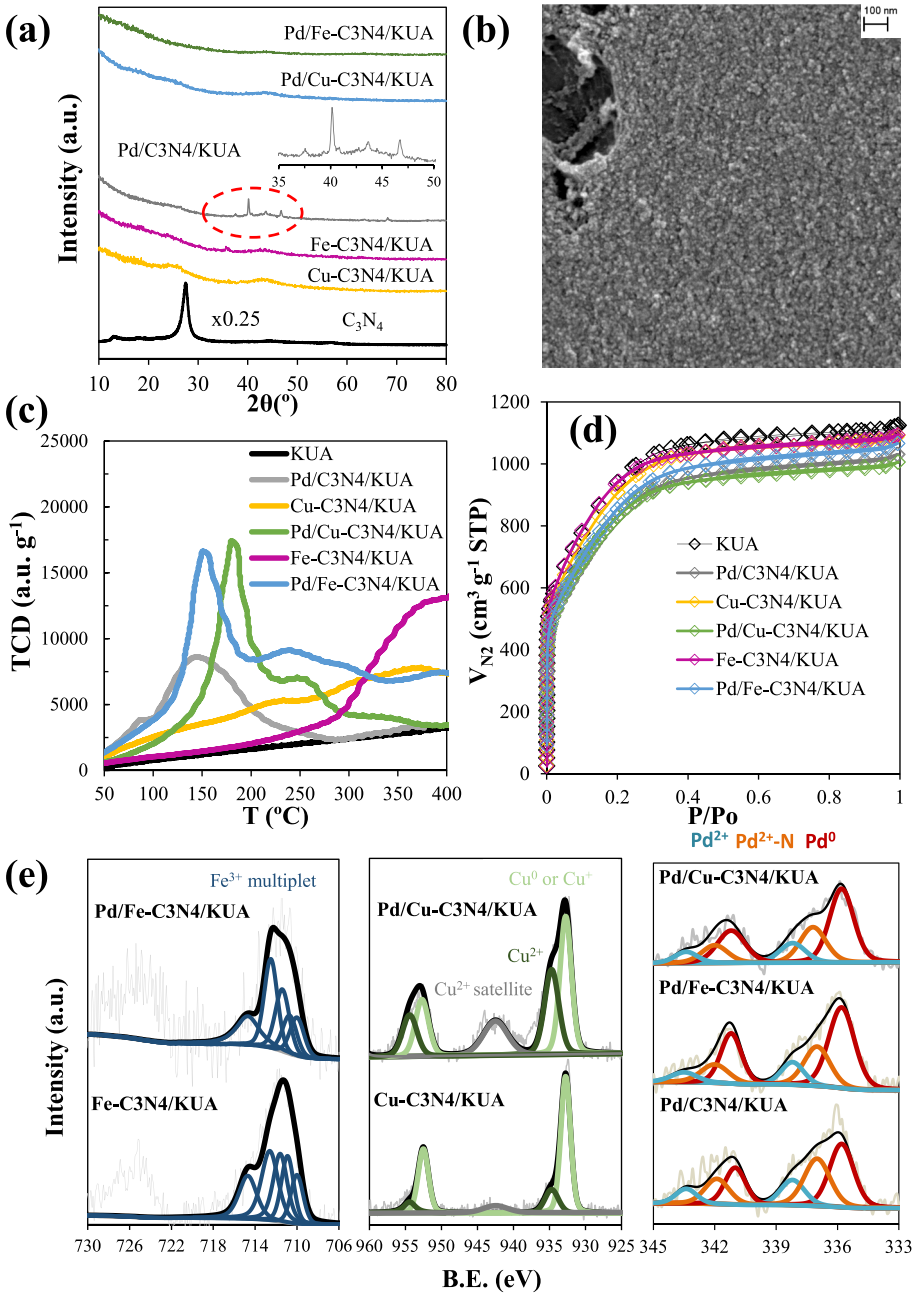

Fig. 1. (a) XRD diffractograms of M−C3N4/KUA and Pd/M−C3N4/KUA samples compared to bare C_3N_4, (b) FESEM image of KUA, (c) TPR-H_2 profiles, (d) N_2 adsorption–desorption isotherms, and (e) Fe 2p, Cu 2p, and Pd 3d XPS spectra of the samples.

relative proportion of Cu^{2+} increases from 32 % to 42 %. That may be due to the possible electron transfer from Cu to Pd caused by the higher electronegativity of Pd. Pd 3d spectra were deconvoluted with the contribution of Pd^0 (335.8 eV), Pd^{2+}-N (337.0 eV) and Pd^{2+} as Pd $(O_2CCH_3)_2$ (338.2 eV) [26,27,57–59]. In Fig. 1e, it can be observed that when Pd NPs are prepared directly over C3N4/KUA, an important amount of Pd remains as Pd^{2+} even though the molar ratio of Pd:$NaBH_4$ used in the synthesis was 1:5. It has been reported that N atoms can stabilise the Pd^{2+} species [26], therefore some Pd^{2+} species may have been stabilised on the basic Lewis sites of the C_3N_4. On the other hand, Pd/M−C3N4/KUA samples present a higher percentage of Pd^0 compared to Pd/C3N4/KUA, because the interaction of Pd atoms with the basic sites is probably weaker. Furthermore, in Pd/Cu-C3N4/KUA sample, the possible electron transfer from Cu to Pd could also be responsible for the larger proportion of reduced Pd species present in Pd/Cu-C3N4/KUA compared to Pd/C3N4/KUA. The different electronic properties of Pd species in the samples and the presence of oxidised Cu species may be related to the interaction between the Pd NPs and the transition metal in the samples.

TEM micrographs are included in Fig. 2. TEM images for Cu-C3N4/KUA and Fe-C3N4/KUA (Fig. 2b,c) did not show metal nanoparticles. However, small black dots were observed in the Pd-containing electrocatalysts (Fig. 2d-f), which are attributed to the presence of Pd NPs in those samples. The average NP size determined for Pd/C3N4/KUA was 4.7 ± 1.5 nm. Such relatively small average NP size can be related to the effect of N basic sites of C_3N_4 and the high porosity of KUA (S_{BET} 3180 m^2/g, V_{DR} 1.57 cm^3/g, and V_T 1.65 cm^3/g). However, as can be seen in the histogram for the NP size distribution of Fig. 2d, the size distribution determined in sample Pd/C3N4/KUA was wider and NPs with sizes up to ~ 9 nm were formed. Interestingly, the average Pd nanoparticle size

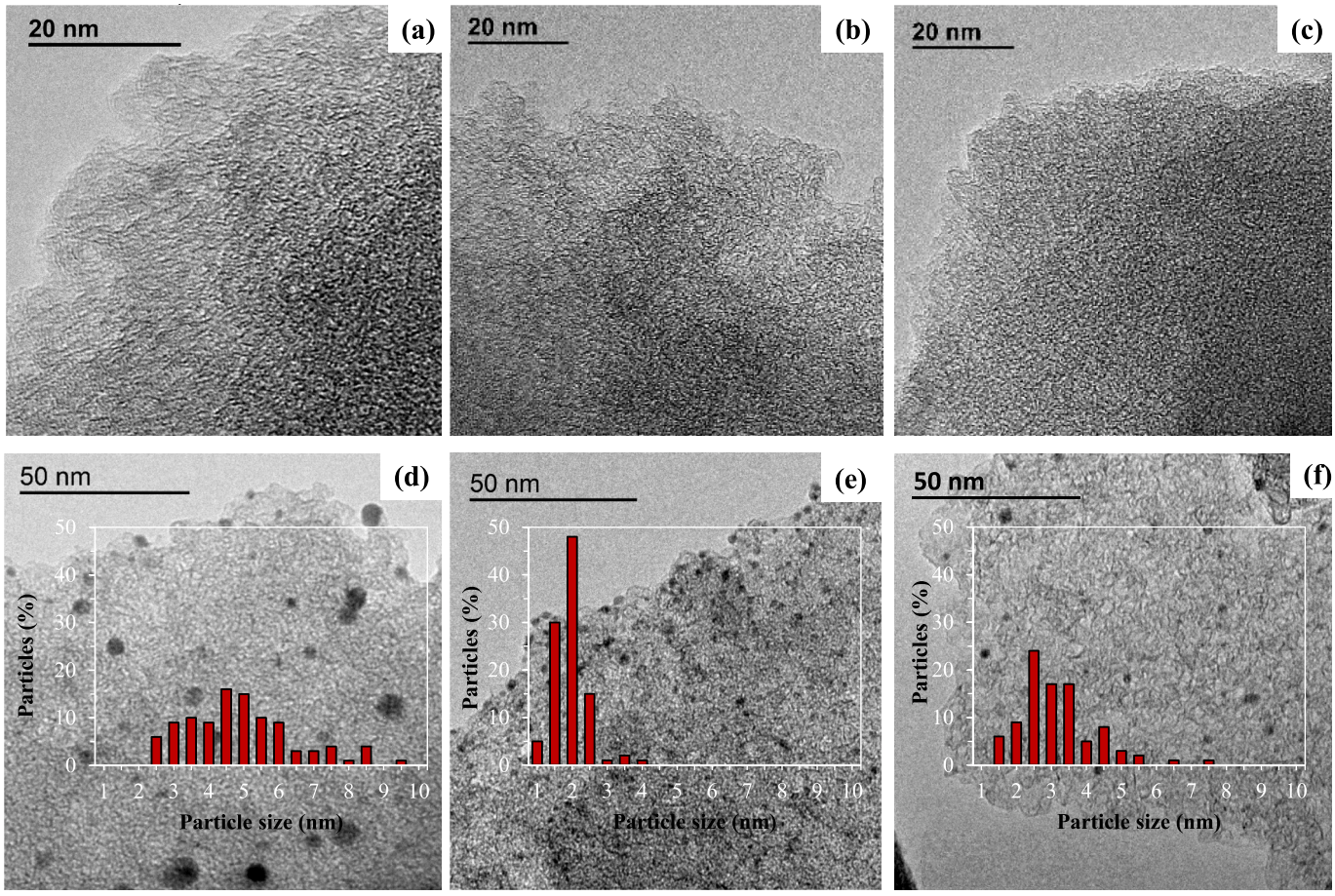

Fig. 2. TEM images and particle size distribution of (a) KUA (b) Cu-C3N4/KUA, (c) Fe-C3N4/KUA, (d) Pd/C3N4/KUA, (e) Pd/Cu-C3N4/KUA and (f) Pd/Fe-C3N4/KUA samples.

of Pd/Cu-C3N4/KUA and Pd/Fe-C3N4/KUA was much smaller (1.7 ± 0.5 nm and 2.9 ± 1.1 nm, respectively), which might suggest that, during the synthesis, Pd atoms may have experienced a strong interaction with the highly dispersed transition metals anchored to C_3N_4, especially with Cu. The TEM results are in quite good agreement with the XRD observations.

3.2. Computational calculations

In order to obtain some insights about the important differences observed experimentally when synthesising Pd NPs over C3N4/KUA or M−C3N4/KUA, the stabilisation of an 8-atom Pd cluster when interacting with a C_3N_4 macromolecule was studied by DFT calculations. The optimised structure of the Pd(8) cluster is shown in Fig. S2a and agrees with that proposed by Nava et al [60]. The interaction of Pd(8) with the C_3N_4 macromolecule is produced by 2 Pd atoms bonding 2 N atoms from different heptazine units. The third heptazine leans slightly down, precluding a major coordination with the basic central nitrogen atoms (Fig. S2b). The interaction energy calculated for Pd(8)-C3N4 was −3.1 eV. Interestingly, the interaction energies calculated for Pd(8)Cu-C3N4 and Pd(8)Fe-C3N4 were substantially more intense (-4.9 eV and −5.1 eV, respectively). These results completely agree with the particle size distribution observed experimentally, which has been strongly influenced by the presence of highly dispersed Fe or Cu, allowing a smaller particle size with a narrower distribution. The results suggest that, although Pd nanoparticles are known to perform with high activity towards HER and oxygen reactions, the preparation of these catalysts may be limited by the low anchoring energy due to the small interaction with the support. Therefore, this is an example on how these limitations can be overcome by boosting the interaction using highly dispersed transition metals-N_x sites.

3.3. Electrochemical characterization of electrocatalysts for ORR, HER and OER

CV experiments are shown in Fig. S5. All the samples showed the typical rectangular profiles of porous carbon materials. The samples containing C_3N_4 showed a more rectangular profile due to its electrical conductivity as has been reported in previous works[13,42]. Due to the large value of the double layer charge, faradaic processes corresponding to metals were not clearly observed.

The results for the ORR characterisation are displayed in Fig. 3 and Table 2. It was observed that Pd-free M−C3N4/KUA samples themselves presented high activities with E_{ONSET} potentials close to 0.9 V vs. RHE. The selectivity towards the formation of H_2O was limited at a number of electrons transferred of 3.70 for Cu-C3N4/KUA and 3.57 for Fe-C3N4/KUA. Even though a small XRD contribution corresponding to iron oxide could be detected in Fe-C3N4/KUA, the electrocatalytic activity displayed by that sample is mainly related to Fe-N_x sites instead of iron oxide nanoparticles. This is because the activity towards the ORR for a material based on iron oxide over KUA (also ~ 1 wt% of Fe) has already been studied in previous works [13], showing a completely different performance (E_{onset} of 0.81 V and 2.9 the number of electrons transferred at 0.65 V). On the other hand, Pd/C3N4/KUA displayed better selectivity towards the 4-electron pathway (a number of electrons transferred of 3.75). The limited selectivity may be related to the low metal loading, allowing at high overpotentials some carbon or C_3N_4 sites to perform through a 2-electron pathway. Interestingly, both Pd/

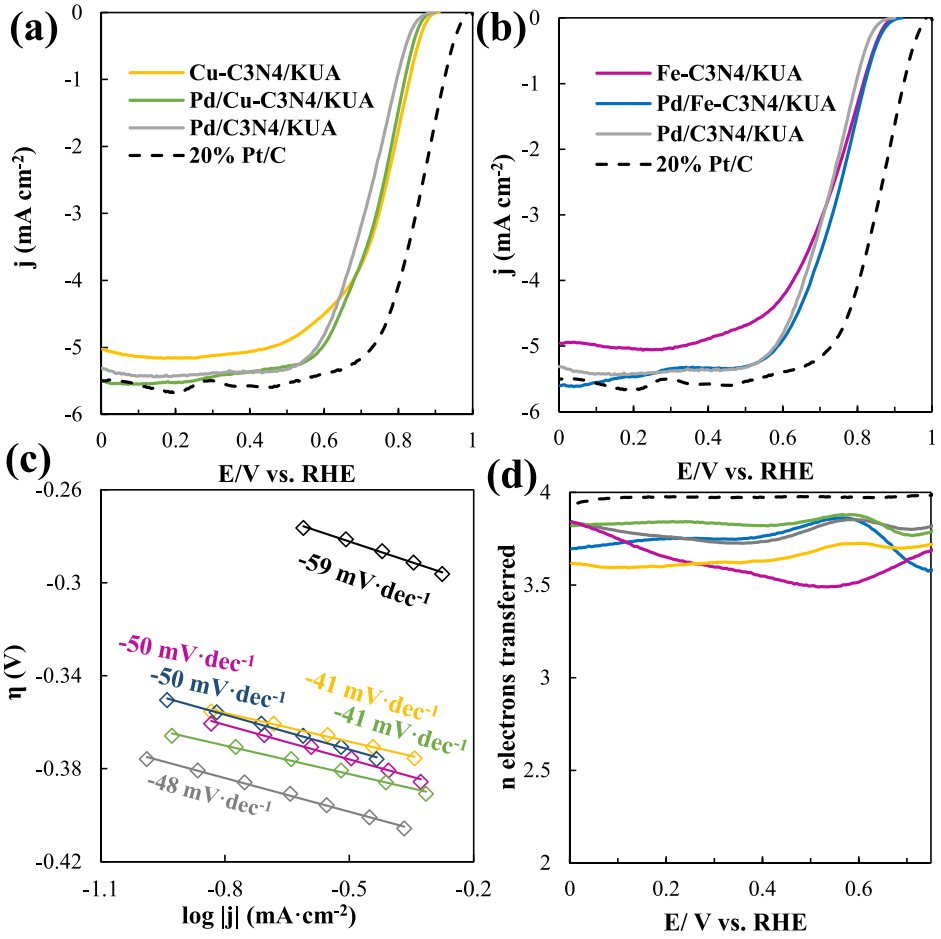

Fig. 3. (a,b) LSV curves and (c) Tafel plots and (d) number of electrons transferred for M−C3N4/KUA and Pd/M−C3N4/KUA samples at 5 mV/s and 1600 rpm in an O_2-saturated 0.1 M KOH solution compared to commercial Pt/C catalyst.

Table 2
Parameters obtained from LSV curves for ORR, OER and HER.

Catalyst	$E_{ONSET\ ORR}$ / $E_{1/2}$ (V)	Tafel slope ORR (mV dec^{-1})	n (at E = 0.65 V)	$E_{ONSET\ OER}$ (V)	Tafel slope OER (mV dec^{-1})	Bifunctional index (V)	$E_{ONSET\ HER}$ (mV)	Tafel slope HER (mV dec^{-1})
20 % Pt/C	0.97 / 0.85	−59	3.97	–	–	–	−36	−26
RuO_2	–	–	–	1.57	226	–	–	–
Cu-C3N4/KUA	0.88/ 0.77	−41	3.70	1.70	217	0.82	−383	−258
Fe-C3N4/KUA	0.88 / 0.73	−50	3.57	1.69	190	0.81	−358	−240
Pd/C3N4/KUA	0.86 / 0.72	−48	3.75	1.65	218	0.79	−193	−91
Pd/Cu-C3N4/KUA	0.87 / 0.75	−41	3.83	1.65	127	0.78	−145	−77
Pd/Fe-C3N4/KUA	0.89 / 0.74	−50	3.82	1.56	128	0.67	−194	−114

*E_{ONSET} potentials are at j_{ORR} = -0.05 mA cm^{-2}; j_{OER} = 10 mA cm^{-2}; j_{HER} = -10 mA cm^{-2}.

M−C3N4/KUA samples not only maintained the high activities of M−C_3N_4 sites (for Pd/Fe-C3N4/KUA even increased), but also the selectivity increased compared to Pd/C3N4/KUA, showing, therefore, a synergistic effect towards the ORR (Fig. 3d and Table 2). Tafel slope plots (Fig. 3c) revealed that the kinetic region of the reaction might be controlled by the M−C_3N_4 sites since the slope values calculated were similar for the respective M−C3N4/KUA and Pd/M−C3N4/KUA samples.

Fig. 4a shows the LSV curves registered for HER using the studied samples and the commercial Pt/C catalyst. As can be seen, the activity of both Fe-C3N4/KUA and Cu-C3N4/KUA was poor, which is probably due to the low metal content in the samples. The superior behaviour of Fe sites towards HER was observed comparing the performance of both samples, which is in agreement with the results previously reported elsewhere [61–63]. As for the Pd-containing electrocatalysts, Pd/Fe-C3N4/KUA and Pd/C3N4/KUA have very similar behaviour (Fig. 4a and Table 2), regardless of the different average NP size. In addition, the calculated Tafel slope is higher for Pd/Fe-C3N4/KUA sample (Fig. S6a), suggesting that Fe sites might not be playing an important role, and the reaction seems to be determined by Pd species which have a high electrocatalytic activity for this reaction. On the contrary, the presence of Cu species results in a decrease in the E_{ONSET} value of almost 50 mV,

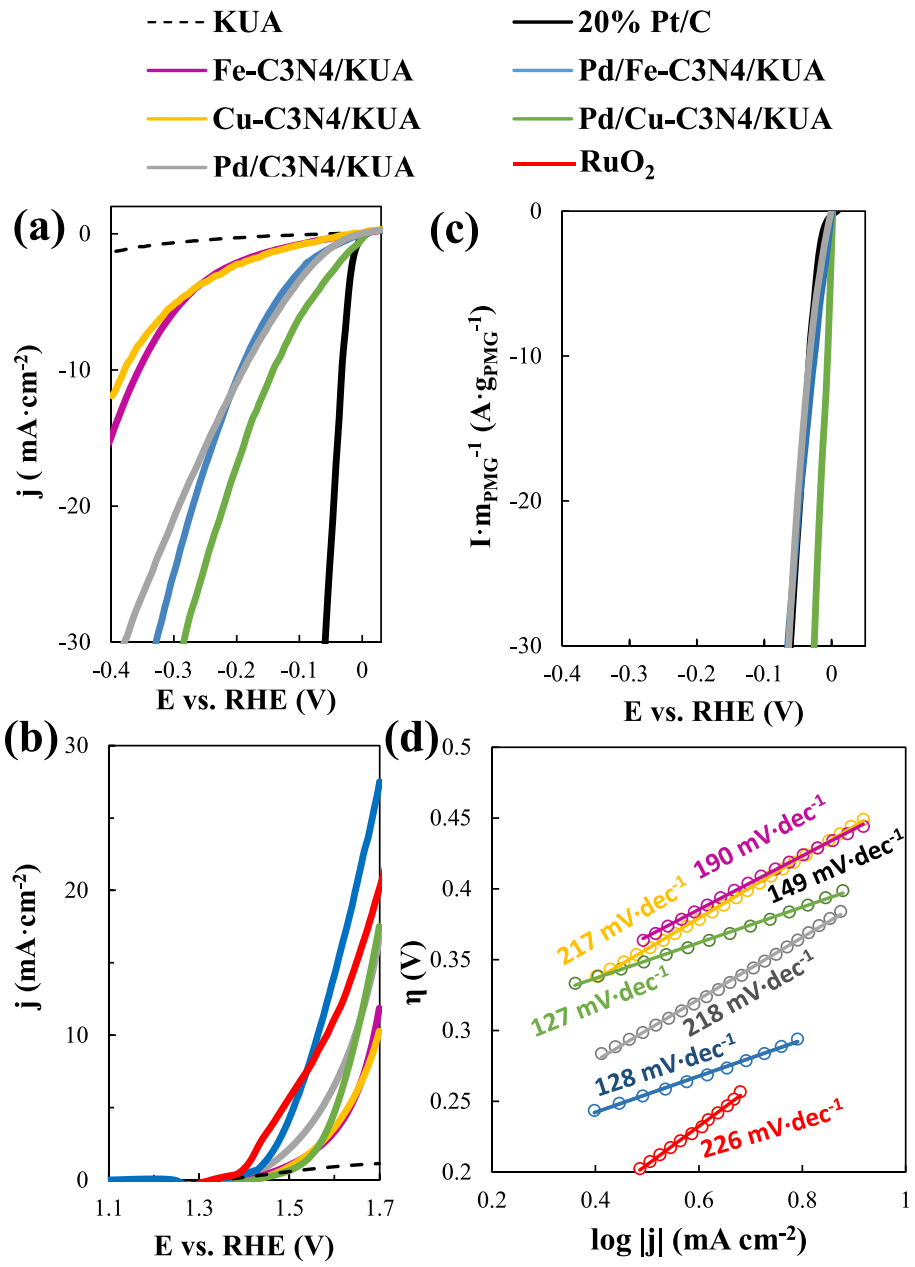

Fig. 4. (a-b) LSV curves for HER and OER, (c) mass activity for HER and (d) OER Tafel plots for M−C3N4/KUA and Pd/M−C3N4/KUA samples at 5 mV/s in N_2-saturated 1 M KOH solution compared to commercial Pt/C and RuO_2 catalysts.

reaching an excellent overpotential (Fig. 4a and Table 2). The observed activity might be a result of the decrease in the average size of Pd NPs in the presence of Cu sites although some additional effects should not be ruled out. For instance, Pd-Cu bimetallic catalysts have been reported as exceptional active phases towards the HER [19,21–23]. In these investigations, a similar modification in the Tafel slope, indicating a better electron transfer in Pd-Cu/C samples than in Pd/C catalysts, was also observed. The lowest value of the Tafel slope calculated for Pd/Cu-C3N4/KUA indicates that a different mechanism might be occurring in this sample compared to the other catalysts and that the electron transfer is superior in this material (Fig. S6a). Finally, mass activity (Fig. 4c) and TOF (Fig. S6b) showed that the current produced per gram (mass activity) or per mole (TOF) of PMG was superior in Pd/Cu-C3N4/KUA than in the commercial Pt/C electrocatalyst in all the potential range studied because of the better atomic efficiency reached.

Long-term durability in HER was evaluated for the best sample (Pd/Cu-C3N4/KUA) by performing a 20 h chronoamperometric test (Fig. S7). After the stability test, the sample showed lower activity. This catalytic activity decay was mainly related to metal leaching as no significant changes were observed between the fresh and used electrodes by TEM or FESEM (Fig. S7b-c). The amount of metal detected by ICP in the used electrode revealed a 19 and 27 % loss of Pd and Cu, respectively, which indicates that bimetallic corrosion may be taking place. The long-term durability may be improved by high-temperature treatment for better anchoring of Cu sites before introducing Pd.

OER was also evaluated in 1 M KOH solution (Fig. 4b). For this reaction, M−C3N4/KUA samples presented very similar performance, although the Tafel slope was lower for Fe-C3N4/KUA sample, indicating better electron transfer. For Pd samples, notwithstanding that the E_{ONSET} value was equivalent for Pd/C3N4/KUA and Pd/Cu-C3N4/KUA samples, the Tafel slope was significantly lower than for the sample with Cu sites, allowing a lower overpotential for higher currents. For Pd/Fe-C3N4/KUA sample, an impressive change of 100 mV in the E_{ONSET} was observed. Such an enhancement cannot be attributed to the

available Pd surface sites in Pd/Fe-C3N4/KUA (i.e., Pd/Fe-C3N4/KUA had larger Pd NPs than Pd/Cu-C3N4/KUA and hence a lower proportion of Pd surface sites). Since Pd and Fe catalysts showed poor activities separately, a synergistic effect due to a Pd-Fe interaction is observed in Pd/Fe-C3N4/KUA. Interestingly, although Pd/M−C3N4/KUA samples showed very different activity, the Tafel slope calculated for these samples is equivalent and close to 120 mV dec^{-1}. That may indicate that, for the OER, Pd-Fe and Pd-Cu sites are probably carrying out the reaction via similar mechanisms through the formation of species in the surface of the active phase, which are rather different from that for Pd/C3N4/KUA sample (Tafel slope 218 mV dec^{-1}) [64].

In order to compare the performance of Pd/Fe-C3N4/KUA with those published in the literature, a table has been included in the supporting information (Table S1). The catalytic performance towards the ORR is interesting compared to the commercial Pd/C (10 wt% of Pd), and very interesting for the OER, where the performance is comparable to other electrocatalysts with much higher metal content.

The current increase observed for gas evolution reactions (HER and OER) for these catalysts was not as sharp as that observed for other materials with similar E_{ONSET} in these reactions [19–23] or for Pt/C in HER (Fig. 4a). However, the current drop seen in the LSV curves for ORR, as well as the Tafel slope values, were comparable to Pt/C. For the ORR, micropores themselves may act as nanoreactors that promote the reaction rate due to an increase in the O_2 concentration near the active sites [65,66]. However, for gas evolution reactions, the opposite effect might be occurring, and the generated gas is probably detained in the micropores due to the high adsorption potential and might result in higher overpotentials. This is a factor that would not affect non-porous materials such as carbon blacks.

HER, ORR and OER were also studied by DFT calculations. In order to speed up the calculations, the clusters consisted of a single Pd-atom (Fig. S8 and Fig. S9) what makes the calculations preliminary and qualitative but can be useful for comparison purposes among the materials. Energy diagrams are shown in Fig. S10. It can be observed that the presence of Fe or Cu strongly modifies the energy diagrams because of the major electron density in the Pd atom. Some of the reaction intermediates as the HO* for ORR or H* for HER showed higher stabilisation in presence of Cu or Fe. A detailed description of the diagrams is included in the Supporting Information. Periodic calculations for the catalytic activity should be performed for higher accuracy, but the results obtained suggest important alterations in the catalytic activity, which agree with the changes observed experimentally, especially for HER and OER.

3.4. Application in ZAB

From the ORR and OER results, Pd/Fe-C3N4/KUA electrocatalyst was selected for the ZAB tests since it displayed the best performance and bifunctional character, (i.e., lower bifunctional index; See Table 2). It was shown that Pd NPs improve the selectivity in the ORR towards the desired 4-electron path and, for the OER, an important synergistic effect exists between both elements obtaining a superior performance than the other catalysts.

Fig. 5 depicts the ZAB charge–discharge measurements for 250 cycles (Fig. 5a) and the galvanostatic discharge experiments (Fig. 5b) for the ZABs built with Pd/Fe-C3N4/KUA and commercial Pt/C mixed 50:50 in weight with RuO_2 as oxygen-reactions electrocatalysts. The charge–discharge experiment showed that, during the first 10 h, the sample reached a performance similar to that of the Pt/C + RuO_2 catalyst towards the ORR. In fact, the cell potential at the discharge was equivalent at t = 10 h (Table 3). In addition, the selected sample showed low and stable overpotential in the charging process compared to the Pt/C + RuO_2 catalyst. After 25 h, both electrocatalysts showed constant potentials at the discharge. It can be observed that the cell voltage for the ZAB containing Pd/Fe-C3N4/KUA increased slowly with time in the charge process, which is probably because of active phase loss. The cell

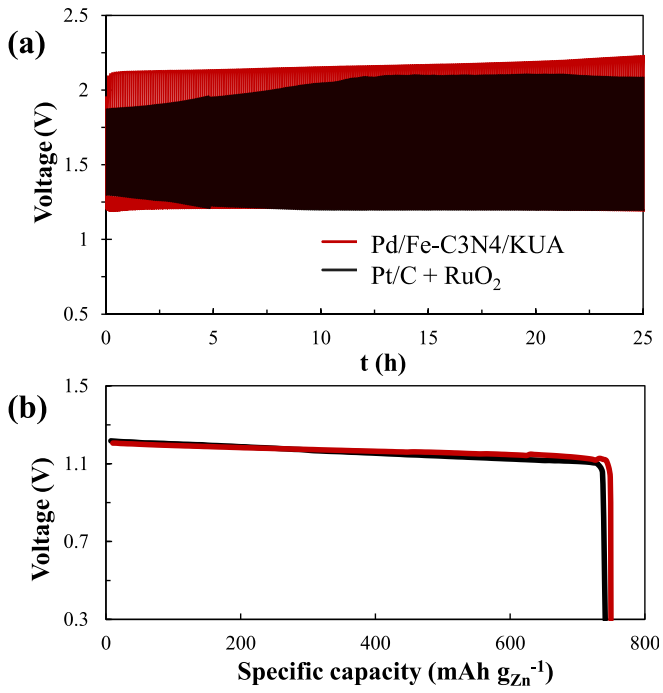

Fig. 5. (a) Charge-discharge experiments of 250 cycles (3 min charge / 3 min discharge) at 1 mA cm^{-2} and (b) long-time galvanostatic discharge curve at 5 mA cm^{-2} (6 M KOH + 0.2 M $Zn(O_2CCH_3)_2$ solution).

Table 3
Parameters obtained from zinc-air battery tests.

Catalyst	*Cell voltage (V)*				Specific capacity (mAh g_{Zn}^{-1})
	Discharge (After 10 h)	*Charge (After 10 h)*	*Discharge (After 25 h)*	*Charge (After 25 h)*	
Pd/Fe-C3N4/KUA	1.20	2.16	1.19	2.23	750
Pt/C + RuO_2	1.20	2.05	1.20	2.08	740

potential ($V_{charge} - V_{discharge}$) from 10 h to 25 h increased in 80 mV for the ZAB containing Pd/Fe-C3N4/KUA and 30 mV for ZAB containing Pt/C + RuO_2. The results are remarkable considering the big difference in PMG content between these two electrodes studied.

Problems related to the oxidation of the carbon support and the consequent loss of conductivity of the carbon material cannot be ruled out. Working on these conditions of continuous potential tuning, carbon materials can be oxidised and further gasified with a reactivity that will increase with the potential [67,68]. Since electrodes based on carbon materials for metal-air batteries are limited by the oxidation of the carbon material, among other factors, the interesting durability observed for the carbon material used in this work can be explained considering the presence of *N*-containing species since it is known that they may increase the stability potential window [69]. In this specific case, the C_3N_4 domains may grow on or over reactive edge sites and defects of the activated carbon thus improving the electrochemical stability [70,71].

The values obtained of specific capacity from the galvanostatic discharge tests were 750 and 740 mAh g_{Zn}^{-1} for ZABs containing Pd/Fe-C3N4/KUA and Pt/C + RuO_2, respectively. The experiment showed that the voltage of the cell for the Pd/Fe-C3N4/KUA sample and the commercial catalyst was equivalent, and even higher for the Pd/Fe-C3N4/KUA during the last part of the test (Fig. 5b). That indicates that the Pd-Fe catalyst prepared presents a high stability for oxygen

reduction reaction. In Fig. S11 it can be observed that the maximum power density for ZAB containing Pd/Fe-C3N4/KUA is centred at lower current densities than that of Pt/C (46 and 110 mA cm^{-2}, respectively). This might explain the comparable performance in the capacity test at 5 mA cm^{-2} for both electrocatalysts. The performance is remarkable considering the low amount of metal employed in comparison to the commercial catalysts.

To deepen into the stability of Pd/Fe-C3N4/KUA sample for the discharge process (ORR), a durability test was performed with the RRDE electrode (Fig. S12), and the result was compared with that of Fe-C3N4/KUA sample. The sample with Pd presented excellent stability while Fe-C3N4/KUA lost activity and the number of electrons transferred decreased until 3.43 at 0.65 V. Pd/Fe-C3N4/KUA electrode after 200 cycles was analysed by XPS, ICP, FESEM and TEM (Fig. S12c-e). No significant modifications in the morphology were observed and Pd species were mostly present as Pd^{2+} after stability test. Interestingly, the amount of Pd detected by ICP in the used electrode was equivalent to the fresh sample while Fe presented just 18 % of leaching, which might correspond to weakly anchored Fe species not interacting with the C_3N_4 domains, as the activity was highly preserved. Therefore, these results suggest that covering the Fe-N_x sites with Pd NPs may be a very interesting strategy for boosting the durability of these materials towards the ORR.

4. Conclusions

Electrocatalysts based on Pd NPs and highly dispersed Cu or Fe sites on C3N4/super-activated carbon composites were prepared by following a simple and reproducible protocol. It was observed that the properties of the Pd NPs were dependent on the composition of the support. Very small and well-dispersed Pd NPs were detected in Pd/M−C3N4/KUA samples, which was corroborated by XRD measurements and agreed with the higher stabilisation energies calculated by DFT for a Pd(8) cluster interacting with M−C3N4 flakes.

Regarding the electroactivity, the selectivity of Pd NPs for the ORR was found to be excellent towards the 4-electron pathway and the high activity was maintained when supported on Fe or Cu-containing C3N4/KUA. Moreover, Pd/Cu-C3N4/KUA sample showed excellent performance for HER, with an overpotential lower than 150 mV that may be related to the decrease of the Pd particle size and the presence of highly active PdCu-C3N4 sites. On the other hand, Pd/Fe-C3N4/KUA showed superior activity for the OER.

Taking into account the good bifunctionality of Pd/Fe-C3N4/KUA for ORR and OER, that sample was selected as the electrocatalyst to be tested in the ZAB. It was observed that the performance was comparable to that of the commercial Pt/C + RuO_2 catalyst and the high stability during long-time galvanostatic discharge may be related to the effect of the strong interaction of Pd NPs with Fe-C3N4/KUA and the decreased reactivity of the C_3N_4-containing porous carbon.

This study demonstrates the synergistic effect between Pd species and transition metals and shows that transition metals anchored on C_3N_4-based composite materials promote the electroactivity of Pd NPs in HER, ORR and OER due to the interaction between both species. However, the selection of the transition metal is key for modifying the electronic structure of Pd species and, thus, the electrocatalytic activity towards and specific reaction.

Although the materials prepared in this work are based on Pd, the content of Pd in the electrodes prepared for the ZAB application was very low (~0.013 mg cm^{-2}), much lower than the maximum loading proposed by the U.S. DOE for fuel cells for example (0.125 mg cm^{-2}) and also lower than that used for other Pd-based materials in the literature (see Table S1 in the Supporting Information). The results are remarkable considering the very low loading (e.g. ~ 10 times less than commercial Pd/C). Therefore, due to the low content of PGM, the materials prepared in this work can be considered as cost-effective and highly promising for these electrochemical energy production devices.

The designed electroactive materials can constitute an alternative to the historically most investigated Pt-based systems and pave the way for the designing of new cost-effective multifunctional electrocatalysts with tailored performances by virtue of the proper selection of both a second metal and support. This is a topic which should be further investigated paying attention to both single site and nanoparticles alloys as catalysts, in order to understand in detail the nature of the interaction between the metal elements and the reactants and products.

CRediT authorship contribution statement

G. Alemany-Molina: Data curation, Formal analysis, Investigation, Methodology, Writing – original draft. **M. Navlani-García:** Formal analysis, Investigation, Methodology, Writing – original draft. **J. Juan-Juan:** Data curation, Formal analysis, Investigation. **E. Morallón:** Conceptualization, Formal analysis, Funding acquisition, Investigation, Methodology, Supervision, Writing – review & editing. **D. Cazorla-Amorós:** Conceptualization, Formal analysis, Funding acquisition, Investigation, Methodology, Supervision, Validation, Writing – review & editing.

Declaration of competing interest

The authors declare that they have no known competing financial interests or personal relationships that could have appeared to influence the work reported in this paper.

Data availability

Data will be made available on request.

Acknowledgments

The authors would like to thank PID2021-123079OB-I00 project funded by MCIN/AEI/10.13039/501100011033 and “ERDF A way of making Europe”. G. Alemany-Molina thanks Ministerio de Universidades for the FPU20/03969 grant. M. Navlani-García acknowledges the Ramón y Cajal contract (RYC2021-034199-I) funded by MCIN/AEI/10.13039/501100011033 and the European Union «NextGenerationEU»/PRTR».

Appendix A. Supplementary data

Supplementary data to this article can be found online at https://doi.org/10.1016/j.jcis.2024.01.057.

References

[1] L.M. Gandía, G. Arzamendi, P.M. Diéguez, Renewable hydrogen energy: an overview, in: L.M. Gandía, G. Arzamendi, P.M. Diéguez (Eds.), Renewable Hydrogen Technologies: Production, Purification, Storage, Applications and Safety, Elsevier, Amsterdam, 2013, pp. 1–18.
[2] X. Zhang, X. Cheng, Q. Zhang, Nanostructured energy materials for electrochemical energy conversion and storage: a review, J. Energy Chem. 25 (2016) 967–984, https://doi.org/10.1016/j.jechem.2016.11.003.
[3] Y. Li, H. Dai, Recent advances in Zinc-air batteries, Chem. Soc. Rev. 43 (2014) 5257–5275, https://doi.org/10.1039/c4cs00015c.
[4] W. Yu, W. Shang, P. Tan, B. Chen, Z. Wu, H. Xu, Z. Shao, M. Liu, M. Ni, Toward a new generation of low cost, efficient, and durable metal-air flow batteries, J. Mater. Chem. a. 7 (2019) 26744–26768, https://doi.org/10.1039/c9ta10658h.
[5] M. Gabbasa, K. Sopian, A. Fudholi, N. Asim, A review of unitized regenerative fuel cell stack: Material, design and research achievements, Int. J. Hydrogen Energy. 39 (2014) 17765–17778, https://doi.org/10.1016/j.ijhydene.2014.08.121.
[6] Z. Yang, H. Nie, X. Chen, X. Chen, S. Huang, Recent progress in doped carbon nanomaterials as effective cathode catalysts for fuel cell oxygen reduction reaction, J. Power Sources. 236 (2013) 238–249, https://doi.org/10.1016/j.jpowsour.2013.02.057.
[7] H.A. Gasteiger, J.E. Panels, S.G. Yan, Dependence of PEM fuel cell performance on catalyst loading, J. Power Sources. 127 (2004) 162–171, https://doi.org/10.1016/j.jpowsour.2003.09.013.

[8] C. Sealy, The problem with platinum, Mater. Today. 11 (2008) 65–68, https://doi.org/10.1016/S1369-7021(08)70254-2.
[9] T. Kou, S. Wang, Y. Li, Perspective on high-rate alkaline water splitting, ACS Mater. Lett. 3 (2021) 224–234, https://doi.org/10.1021/acsmaterialslett.0c00536.
[10] M. Zeng, Y. Li, Recent advances in heterogeneous electrocatalysts for the hydrogen evolution reaction, J. Mater. Chem. a. 3 (2015) 14942–14962, https://doi.org/10.1039/c5ta02974k.
[11] J. Knöppel, M. Möckl, D. Escalera-López, K. Stojanovski, M. Bierling, T. Böhm, S. Thiele, M. Rzepka, S. Cherevko, On the limitations in assessing stability of oxygen evolution catalysts using aqueous model electrochemical cells, Nat. Commun. 12 (2021) 1–9, https://doi.org/10.1038/s41467-021-22296-9.
[12] J. Quílez-Bermejo, E. Morallón, D. Cazorla-Amorós, Metal-free heteroatom-doped carbon-based catalysts for ORR. a Critical Assessment about the Role of Heteroatoms, Carbon. 165 (2020) 434–454, https://doi.org/10.1016/j.carbon.2020.04.068.
[13] G. Alemany-Molina, J. Quílez-Bermejo, M. Navlani-García, E. Morallón, D. Cazorla-Amorós, Efficient and cost-effective ORR electrocatalysts based on low content transition metals highly dispersed on C3N4/super-activated carbon composites, Carbon. 196 (2022) 378–390, https://doi.org/10.1016/j.carbon.2022.05.003.
[14] Q. Xue, G. Xu, R. Mao, H. Liu, J. Zeng, J. Jiang, Y. Chen, Polyethyleneimine modified AuPd@PdAu alloy nanocrystals as advanced electrocatalysts towards the oxygen reduction reaction, J. Energy Chem. 26 (2017) 1153–1159, https://doi.org/10.1016/j.jechem.2017.06.007.
[15] Z. Yu, J. Xu, I. Amorim, Y. Li, L. Liu, Easy preparation of multifunctional ternary PdNiP/C catalysts toward enhanced small organic molecule electro-oxidation and hydrogen evolution reactions, J. Energy Chem. 58 (2021) 256–263, https://doi.org/10.1016/j.jechem.2020.10.016.
[16] M. Li, Z. Xia, M. Luo, L. He, L. Tao, W. Yang, Y. Yu, S. Guo, Structural regulation of Pd-based nanoalloys for advanced electrocatalysis, Small Sci. 1 (2021) 2100061, https://doi.org/10.1002/smsc.202100061.
[17] S. Sarkar, S.C. Peter, An overview on Pd-based electrocatalysts for the hydrogen evolution reaction, Inorg. Chem. Front. 5 (2018) 2060–2080, https://doi.org/10.1039/c8qi00042e.
[18] B. Xu, Y. Zhang, L. Li, Q. Shao, X. Huang, Recent progress in low-dimensional palladium-based nanostructures for electrocatalysis and beyond, Coord. Chem. Rev. 459 (2022) 214388, https://doi.org/10.1016/j.ccr.2021.214388.
[19] M. Nunes, D.M. Fernandes, M.V. Morales, I. Rodríguez-Ramos, A. Guerrero-Ruiz, C. Freire, Cu and Pd nanoparticles supported on a graphitic carbon material as bifunctional HER/ORR electrocatalysts, Catal. Today. 357 (2020) 279–290, https://doi.org/10.1016/j.cattod.2019.04.043.
[20] Q. Qu, J.H. Zhang, J. Wang, Q.Y. Li, C.W. Xu, X. Lu, Three-dimensional ordered mesoporous Co3O4 enhanced by Pd for oxygen evolution reaction, Sci. Rep. 7 (2017) 1–9, https://doi.org/10.1038/srep41542.
[21] J. Li, F. Li, S.X. Guo, J. Zhang, J. Ma, PdCu@Pd Nanocube with Pt-like activity for hydrogen evolution reaction, ACS Appl. Mater. Interfaces. 9 (2017) 8151–8160, https://doi.org/10.1021/acsami.7b01241.
[22] Y. Jia, T.H. Huang, S. Lin, L. Guo, Y.M. Yu, J.H. Wang, K.W. Wang, S. Dai, Stable Pd-Cu hydride catalyst for efficient hydrogen evolution, Nano Lett. 22 (2022) 1391–1397, https://doi.org/10.1021/acs.nanolett.1c04840.
[23] S.R. Hosseini, S. Ghasemi, S.A. Ghasemi, Fabrication and performance evaluation of Pd-Cu nanoparticles for hydrogen evolution reaction, ChemistrySelect. 4 (2019) 6854–6861, https://doi.org/10.1002/slct.201901419.
[24] DOE Fuel Cell Technologies Office, 2014 Fuel Cells Technology Market Report (Washington, D.C. 2015), Retrieved from, http://energy.gov/sites/prod/files/2015/10/f27/fcto_2014_market_report.pdf.
[25] L. Liu, A. Corma, Evolution of isolated atoms and clusters in catalysis, Trends Chem. 2 (2020) 383–400, https://doi.org/10.1016/j.trechm.2020.02.003.
[26] D.A. Bulushev, M. Zacharska, E.V. Shlyakhova, A.L. Chuvilin, Y. Guo, S. Beloshapkin, A.V. Okotrub, L.G. Bulusheva, Single isolated Pd2+ cations supported on N-doped carbon as active sites for hydrogen production from formic acid decomposition, ACS Catal. 6 (2016) 681–691, https://doi.org/10.1021/acscatal.5b02381.
[27] J. Chaparro-Garnica, M. Navlani-García, D. Salinas-Torres, E. Morallón, D. Cazorla-Amorós, Highly Stable N-Doped Carbon-Supported Pd-Based Catalysts Prepared from Biomass Waste for H_2 Production from Formic Acid, ACS Sustain. Chem. Eng. 8 (2020) 15030–15043, https://doi.org/10.1021/acssuschemeng.0c05906.
[28] J. Chaparro-Garnica, M. Navlani-García, D. Salinas-Torres, Á. Berenguer-Murcia, E. Morallón, D. Cazorla-Amorós, Efficient production of hydrogen from a valuable CO2-derived molecule: formic acid dehydrogenation boosted by biomass waste-derived catalysts, Fuel. 320 (2022), https://doi.org/10.1016/j.fuel.2022.123900.
[29] S. Zhong, X. Yang, L. Chen, N. Tsumori, N. Taguchi, Q. Xu, Interfacing with Fe-N-C sites boosts the formic acid dehydrogenation of palladium nanoparticles, ACS Appl. Mater. Interfaces. 13 (2021) 46749–46755, https://doi.org/10.1021/acsami.1c14009.
[30] Q. Zhang, J. Guan, Single-atom catalysts for electrocatalytic applications, Adv. Funct. Mater. 30 (2020) 1–53, https://doi.org/10.1002/adfm.202000768.
[31] G.L. Bezemer, J.H. Bitter, H.P.C.E. Kuipers, H. Oosterbeek, J.E. Holewijn, X. Xu, F. Kapteijn, A.J. Van Diilen, K.P. De Jong, Cobalt particle size effects in the Fischer-Tropsch reaction studied with carbon nanofiber supported catalysts, J. Am. Chem. Soc. 128 (2006) 3956–3964, https://doi.org/10.1021/ja058282w.
[32] X. Wei, X. Luo, N. Wu, W. Gu, Y. Lin, C. Zhu, Recent advances in synergistically enhanced single-atomic site catalysts for boosted oxygen reduction reaction, Nano Energy. 84 (2021) 105817, https://doi.org/10.1016/j.nanoen.2021.105817.
[33] S.L. Li, H. Yin, X. Kan, L.Y. Gan, U. Schwingenschlögl, Y. Zhao, Potential of transition metal atoms embedded in buckled monolayer g-C3N4 as single-atom catalysts, Phys. Chem. Chem. Phys. 19 (2017) 30069–30077, https://doi.org/10.1039/c7cp05195f.
[34] Y. Zheng, Y. Jiao, Y. Zhu, Q. Cai, A. Vasileff, L.H. Li, Y. Han, Y. Chen, S.Z. Qiao, Molecule-level g-C3N4 coordinated transition metals as a new class of electrocatalysts for oxygen electrode reactions, J. Am. Chem. Soc. 139 (2017) 3336–3339, https://doi.org/10.1021/jacs.6b13100.
[35] S. An, G. Zhang, T. Wang, W. Zhang, K. Li, C. Song, J.T. Miller, S. Miao, J. Wang, X. Guo, High-density ultra-small clusters and single-atom fe sites embedded in graphitic carbon nitride (g-C3N4) for highly efficient catalytic advanced oxidation processes, ACS Nano. 12 (2018) 9441–9450, https://doi.org/10.1021/acsnano.8b04693.
[36] X. Chen, R. Hu, DFT-based study of single transition metal atom doped g-C3N4 as alternative oxygen reduction reaction catalysts, Int. J. Hydrogen Energy. 44 (2019) 15409–15416, https://doi.org/10.1016/j.ijhydene.2019.04.057.
[37] C. Yang, Z.Y. Zhao, H.T. Wei, X.Y. Deng, Q.J. Liu, DFT calculations for single-atom confinement effects of noble metals on monolayer g-C3N4for photocatalytic applications, RSC Adv. 11 (2021) 4276–4285, https://doi.org/10.1039/d0ra09815a.
[38] M. Navlani-García, D. Salinas-Torres, F.D. Vázquez-Álvarez, D. Cazorla-Amorós, Formic acid dehydrogenation attained by Pd nanoparticles-based catalysts supported on MWCNT-C3N4 composites, Catal. Today. 397–399 (2021) 428–435, https://doi.org/10.1016/j.cattod.2021.07.019.
[39] W.J. Niu, J.Z. He, Y.P. Wang, Q.Q. Sun, W.W. Liu, L.Y. Zhang, M.C. Liu, M.J. Liu, Y. L. Chueh, A hybrid transition metal nanocrystal-embedded graphitic carbon nitride nanosheet system as a superior oxygen electrocatalyst for rechargeable Zn-air batteries, Nanoscale. 12 (2020) 19644–19654, https://doi.org/10.1039/d0nr03987j.
[40] X. Liu, W. Yang, L. Chen, Z. Liu, L. Long, S. Wang, C. Liu, S. Dong, J. Jia, Graphitic carbon nitride (g-C3N4)-derived bamboo-like carbon nanotubes/Co nanoparticles hybrids for highly efficient electrocatalytic oxygen reduction, ACS Appl. Mater. Interfaces. 12 (2020) 4463–4472, https://doi.org/10.1021/acsami.9b18454.
[41] N. Zhang, Y. Gao, L. Ma, Y. Wang, L. Huang, B. Wei, Y. Xue, H. Zhu, R. Jiang, Single transition metal atom anchored on g-C3N4 as an electrocatalyst for nitrogen fixation: a computational study, Int. J. Hydrogen Energy. 48 (2023) 7621–7631, https://doi.org/10.1016/j.ijhydene.2022.09.074.
[42] G. Alemany-Molina, B. Martínez-Sánchez, A. Gabe, T. Kondo, D. Cazorla-Amorós, E. Morallón, Exploring the effect of surface chemistry and particle size of boron-doped diamond powder as catalyst and catalyst support for the oxygen reduction reaction, Electrochim. Acta. 446 (2023) 142121, https://doi.org/10.1016/j.electacta.2023.142121.
[43] D. Lozano-Castelló, M.A. Lillo-Ródenas, D. Cazorla-Amorós, A. Linares-Solano, Preparation of activated carbons from Spanish anthracite - I Activation by KOH, Carbon. 39 (2001) 741–749, https://doi.org/10.1016/S0008-6223(00)00185-8.
[44] W. Zhang, Q. Peng, L. Shi, Q. Yao, X. Wang, A. Yu, Z. Chen, Y. Fu, Merging single-atom-dispersed iron and graphitic carbon nitride to a joint electronic system for high-efficiency photocatalytic hydrogen evolution, Small. 15 (2019) 1–8, https://doi.org/10.1002/smll.201905166.
[45] T.S. Miller, A.B. Jorge, T.M. Suter, A. Sella, F. Corà, P.F. McMillan, Carbon nitrides: synthesis and characterization of a new class of functional materials, Phys. Chem. Chem. Phys. 19 (2017) 15613–15638, https://doi.org/10.1039/c7cp02711g.
[46] J.H. Ramirez, F.J. Maldonado-Hódar, A.F. Pérez-Cadenas, C. Moreno-Castilla, C. A. Costa, L.M. Madeira, Azo-dye Orange II degradation by heterogeneous Fenton-like reaction using carbon-Fe catalysts, Appl. Catal. B Environ. 75 (2007) 312–323, https://doi.org/10.1016/j.apcatb.2007.05.003.
[47] T. Yamashita, P. Hayes, Analysis of XPS spectra of Fe 2+ and Fe 3+ ions in oxide materials, Appl. Surf. Sci. 254 (2008) 2441–2449, https://doi.org/10.1016/j.apsusc.2007.09.063.
[48] L. Xu, X.C. Wu, J.J. Zhu, Green preparation and catalytic application of Pd nanoparticles, Nanotechnol. 19 (2008) 305603, https://doi.org/10.1088/0957-4484/19/30/305603.
[49] M.C. Román-Martínez, D. Cazorla-Amorós, A. Linares-Solano, C.S.M. de Lecea, Tpd and TPR characterization of carbonaceous supports and Pt/C catalysts, Carbon. 31 (1993) 895–902, https://doi.org/10.1016/0008-6223(93)90190-L.
[50] E. Raymundo-Piñero, D. Cazorla-Amorós, A. Linares-Solano, J. Find, U. Wild, R. Schlögl, Structural characterization of N-containing activated carbon fibers prepared from a low softening point petroleum pitch and a melamine resin, Carbon. 40 (2002) 597–608, https://doi.org/10.1016/S0008-6223(01)00155-5.
[51] W. Ju, A. Bagger, G.P. Hao, A.S. Varela, I. Sinev, V. Bon, B. Roldan Cuenya, S. Kaskel, J. Rossmeisl, P. Strasser, Understanding activity and selectivity of metal-nitrogen-doped carbon catalysts for electrochemical reduction of CO2, Nat. Commun. 8 (2017) 1–9, https://doi.org/10.1038/s41467-017-01035-z.
[52] A.P. Grosvenor, B.A. Kobe, M.C. Biesinger, N.S. McIntyre, Investigation of multiplet splitting of Fe 2p XPS spectra and bonding in iron compounds, Surf. Interface Anal. 36 (2004) 1564–1574, https://doi.org/10.1002/sia.1984.
[53] Atkins, Overton, Rourke, Weller, Armstrong and Hagerman. Inorganic Chemistry, Fifth ed., W. H. Freeman and Company, New York, 2010.
[54] J.X. Flores-Lasluisa, J. Quílez-Bermejo, A.C. Ramírez-Pérez, F. Huerta, D. Cazorla-Amorós, E. Morallón, Copper-doped cobalt spinel electrocatalysts supported on activated carbon for hydrogen evolution reaction, Materials. 12 (2019) 1302, https://doi.org/10.3390/ma12081302.
[55] F. Yang, X. Mao, M. Ma, C. Jiang, P. Zhang, J. Wang, Q. Deng, Z. Zeng, S. Deng, Scalable strategy to fabricate single Cu atoms coordinated carbons for efficient electroreduction of CO2 to CO, Carbon 168 (2020) 528–535, https://doi.org/10.1016/j.carbon.2020.06.088.
[56] B. Wu, R. Yang, L. Shi, T. Lin, X. Yu, M. Huang, K. Gong, F. Sun, Z. Jiang, S. Li, L. Zhong, Y. Sun, Cu single-atoms embedded in porous carbon nitride for selective

oxidation of methane to oxygenates, Chem. Commun. 56 (2020) 14677–14680, https://doi.org/10.1039/d0cc06492k.
[57] J. García-Aguilar, M. Navlani-García, Á. Berenguer-Murcia, K. Mori, Y. Kuwahara, H. Yamashita, D. Cazorla-Amorós, Evolution of the PVP-Pd surface interaction in nanoparticles through the case study of formic acid decomposition, Langmuir. 32 (2016) 12110–12118, https://doi.org/10.1021/acs.langmuir.6b03149.
[58] Y. Wu, M. Wen, M. Navlani-García, Y. Kuwahara, K. Mori, H. Yamashita, Palladium nanoparticles supported on titanium-doped graphitic carbon nitride for formic acid dehydrogenation, Chem. - an Asian J. 12 (2017) 860–867, https://doi.org/10.1002/asia.201700041.
[59] F.S. Golub, S. Beloshapkin, A.V. Gusel'Nikov, V.A. Bolotov, V.N. Parmon, D. A. Bulushev, Boosting hydrogen production from formic acid over Pd catalysts by deposition of N-Containing precursors on the carbon support, Energies. 12 (2019) 1–13, https://doi.org/10.3390/en12203885.
[60] P. Nava, M. Sierka, R. Ahlrichs, Density functional study of palladium clusters, Phys. Chem. Chem. Phys. 5 (2003) 3372–3381, https://doi.org/10.1039/b303347c.
[61] H. Liu, X. Peng, X. Liu, Single-atom catalysts for the hydrogen evolution reaction, ChemElectroChem. 5 (2018) 2963–2974, https://doi.org/10.1002/celc.201800507.
[62] Y. Xue, B. Huang, Y. Yi, Y. Guo, Z. Zuo, Y. Li, Z. Jia, H. Liu, Y. Li, Anchoring zero valence single atoms of nickel and iron on graphdiyne for hydrogen evolution, Nat. Commun. 9 (2018), https://doi.org/10.1038/s41467-018-03896-4.
[63] F. Shen, Y. Wang, G. Qian, W. Chen, W. Jiang, L. Luo, S. Yin, Bimetallic iron-iridium alloy nanoparticles supported on nickel foam as highly efficient and stable catalyst for overall water splitting at large current density, Appl. Catal. B Environ. 278 (2020) 119327, https://doi.org/10.1016/j.apcatb.2020.119327.
[64] T. Shinagawa, A.T. Garcia-Esparza, K. Takanabe, Insight on Tafel slopes from a microkinetic analysis of aqueous electrocatalysis for energy conversion, Sci. Rep. 5 (2015) 1–21, https://doi.org/10.1038/srep13801.
[65] A. Gabe, R. Ruiz-Rosas, C. González-Gaitán, E. Morallón, D. Cazorla-Amorós, Modeling of oxygen reduction reaction in porous carbon materials in alkaline medium. effect of microporosity, J. Power Sources. 412 (2019) 451–464, https://doi.org/10.1016/j.jpowsour.2018.11.075.
[66] T.J. Bandosz, Revealing the impact of small pores on oxygen reduction on carbon electrocatalysts: a journey through recent findings, Carbon. 188 (2022) 289–304, https://doi.org/10.1016/j.carbon.2021.11.071.
[67] Y. Shao, J. Wang, R. Kou, M. Engelhard, J. Liu, Y. Wang, Y. Lin, The corrosion of PEM fuel cell catalyst supports and its implications for developing durable catalysts, Electrochim. Acta. 54 (2009) 3109–3114, https://doi.org/10.1016/j.electacta.2008.12.001.
[68] G. Alemany-molina, B. Martínez-Sánchez, E. Morallón, D. Cazorla-Amorós, The role of oxygen heteroatoms in the surface (electro) chemistry of carbon materials, Carbon Reports. 1 (2022) 162–174, https://doi.org/10.7209/carbon.010405.
[69] M.J. Mostazo-López, R. Ruiz-Rosas, E. Morallón, D. Cazorla-Amorós, Nitrogen doped superporous carbon prepared by a mild method. enhancement of supercapacitor performance, Int. J. Hydrogen Energy. 41 (2016) 19691–19701, https://doi.org/10.1016/j.ijhydene.2016.03.091.
[70] A.Y. Chen, T.T. Zhang, Y.J. Qiu, D. Wang, P. Wang, H.J. Li, Y. Li, J.H. Yang, X. Y. Wang, X.F. Xie, Construction of nanoporous gold/g-C3N4 heterostructure for electrochemical supercapacitor, Electrochim. Acta. 294 (2019) 260–267, https://doi.org/10.1016/j.electacta.2018.10.106.
[71] L.G. Ghanem, M.A. Hamza, M.M. Taha, N.K. Allam, Symmetric supercapacitor devices based on pristine g-C3N4 mesoporous nanosheets with exceptional stability and wide operating voltage window, J. Energy Storage. 52 (2022) 104850, https://doi.org/10.1016/j.est.2022.104850.